

Hierarchical Ni₂P@Ni(OH)₂ Architectures Supported On Carbon Cloth As Battery-Type Electrodes For Hybrid Supercapacitors With Boosting Specific Capacitance and Cycle Stability

Yingying Lan

Northwest University

Hongna Xing

Northwest University

Yan Zong

Northwest University

Yong Sun

Northwest University

Linxue Zhang

Northwest University

Yajing Wang

Northwest University

Xinghua Li

Northwest University

Xinliang Zheng (✉ zhengxl@nwu.edu.cn)

Northwest University <https://orcid.org/0000-0003-3836-2982>

Research Article

Keywords: Ni₂P@Ni(OH)₂ nanosheets, Battery-type electrodes, Hybrid supercapacitor, Energy storage

Posted Date: February 16th, 2021

DOI: <https://doi.org/10.21203/rs.3.rs-194018/v1>

License:  This work is licensed under a Creative Commons Attribution 4.0 International License.

[Read Full License](#)

Version of Record: A version of this preprint was published at Journal of Materials Science: Materials in Electronics on March 1st, 2021. See the published version at <https://doi.org/10.1007/s10854-021-05521->

1 **Hierarchical Ni₂P@Ni(OH)₂ architectures supported on carbon cloth**
2 **as battery-type electrodes for hybrid supercapacitors with boosting**
3 **specific capacitance and cycle stability**

4
5 Yingying Lan^{1,2,#}, Hongna Xing^{1,#}, Yan Zong¹, Yong Sun¹, Linxue Zhang^{1,3}, Yajing
6 Wang¹, Xinghua Li¹, Xinliang Zheng^{1,*}

7
8 ¹ School of Physics, Northwest University, Xi'an, Shaanxi 710127, China.

9 ² Songshan Lake Materials Laboratory, Dongguan, Guangdong 523808, China

10 ³ School of Medical Engineering and Technology, Xinjiang Medical University, Urumqi, Xinjiang
11 830011, China.

12 # These authors contribute equally to this work.

13 * Corresponding author: zhengxl@nwu.edu.cn (X. Zheng)

14
15 **Abstract**

16 In this work, a novel binder-free electrode, in which three-dimensional porous
17 Ni₂P@Ni(OH)₂ nanosheet arrays were in-situ grown on carbon cloth (CC), is
18 rationally designed for supercapacitor applications. In comparison with Ni₂P@CC, the
19 Ni₂P@Ni(OH)₂@CC electrode represents superior electrochemical characteristics: the
20 gravimetric capacitance and areal capacitance are boosted to be 632 C g⁻¹ and 0.73 C
21 cm⁻² at 1 mA cm⁻², about 2 and 2.7 times larger than those of Ni₂P@CC (321 C g⁻¹
22 and 0.27 C cm⁻²), respectively; the rate capability is improved to be 63.3% from 1 to

1 10 mA cm⁻², about 1.5 times larger than Ni₂P@CC (42.9%); the cycle stability is
2 enhanced to be 81.4% after 1000 cycles, about 1.6 times larger than Ni₂P/CC (51.8%).
3 The assembly Ni₂P@Ni(OH)₂@CC//AC hybrid supercapacitor device shows high
4 energy density of 23.5 Wh kg⁻¹ at a power density of 1158.0 W kg⁻¹ and good cycling
5 stability of 75.2% maintenance after 5000 cycles. Benefiting from the combined
6 advantages of high electronic conductivity and large specific capacitance of Ni₂P,
7 superior anion exchanging/intercalating capacity of Ni(OH)₂, excellent flexibility of
8 carbon cloth and special hierarchical architecture with large surface area, the
9 Ni₂P@Ni(OH)₂@CC electrode is promised to be a good candidate for
10 supercapacitors.

11 **Keywords:** Ni₂P@Ni(OH)₂ nanosheets; Battery-type electrodes; Hybrid
12 supercapacitor; Energy storage

13

14 **1 Introduction**

15 As the depletion of non-renewable fossil fuels and consequent environmental
16 pollutions are ever-increasing serious, the exploration of clean and renewable energy
17 sources, such as solar, wind, tide and geothermal has drawn growing concerns [1-4].

18 However, these energy sources are shackled by time or region, and the utilization
19 efficiency is relative low [5-7]. Developing novel high-efficient energy storage and
20 conversion systems are urgently demanded. Supercapacitors has attracted widespread
21 attention, owing to their specific features such as higher power density than batteries,
22 larger specific energy than conventional capacitors, reliable cycling stability, fast

1 charge/discharge rates, safety, low cost and environmental friendliness [8-11].
2 However, the low energy density of supercapacitors limits its practical application
3 [12-14]. According to the energy storage mechanism, supercapacitors can be divided
4 into two types: electrical double-layer capacitors (EDLCs) and pseudocapacitor (PCs)
5 [15-18]. Generally, PCs possess larger energy storage ability than EDLCs, due to that
6 the electrode materials of PCs show rich oxidation states for faradaic redox reactions.
7 The core technology of PCs is exploring novel electrode materials with high specific
8 capacitance.

9 Recently, battery-type electrode materials, especially transition metal compounds,
10 have been widely used for supercapacitors. This is owing to their efficient faradaic
11 redox reactions [19-21]. As a kind of n-type semiconductors, metal phosphides have
12 two types of bonding states: the covalent bonded metal cations can store charges
13 through faradaic redox reactions; the metal bonded atoms can improve the electrical
14 conductivity through free electrons [22]. This specific structure makes metal
15 phosphides possess metalloid property and excellent electrical conductivity.
16 Compared with oxygen atom, phosphorus atom in metal phosphides is more
17 electronegative, which can result in faster electron migration and superior redox
18 activity [23]. These features are beneficial for electron transport that can improve the
19 rate capability [24]. The transition metal phosphides (TMPs) have larger theoretical
20 capacitance and higher electrical conductivity in comparison with the transition metal
21 oxides (TMOs) [25]. Moreover, the nanostructures of TMPs are usually highly
22 tunable for the access of electrolytes, leading to excellent intra- and inter-particle

1 conductivity, which is also important for electrode materials [26]. These intrinsic
2 chemical/physical features make TMPs potential for supercapacitors. Wang *et al.*
3 prepared amorphous Ni-P nanomaterials by a solvothermal route, which show a large
4 specific capacitance of 1595 F g^{-1} at 0.5 A g^{-1} and 71.4% capacitance preserved after
5 1000 cycles [27]. Lu *et al.* fabricated spherical and rod-like Ni_2P nanostructures by
6 hydrothermal-phosphidation two-step process, and found that the rod-like Ni_2P
7 nanostructures have a larger specific capacitance of 799.2 F g^{-1} at 1 A g^{-1} and cycling
8 stability of 68.4% after 2500 cycles [28]. Obviously, the metal phosphides present
9 remarkable electrochemical performance, but their specific capacitance and cycle
10 stability still need to be further improved.

11 Generally, interface construction can introduce interfacial charge migration owing
12 to the generated strain at the interface, which is promised to be an effective way to
13 boost the electrochemical properties of electrode materials [29, 30]. Hierarchical
14 core-shell architectures are proposed to be a kind of hybrid nanostructures that can
15 enlarge the surface/interface area, improve the contact of electrode/electrolyte and
16 shorten the channel of ion diffusion [31-33]. Especially, properly constructing
17 core-shell architectures composited of core with large electrical conductivity and shell
18 with pseudo-capacitivity are promised to be of great significance for supercapacitors
19 [34, 35]. The particular heterostructure may induce internal electric fields and
20 discontinuous charges at the interface, which can enhance the electric/ionic
21 conductivity and improve the redox reaction kinetics. Besides, this core-shell
22 heterostructure can enhance the electron storage/delivery pathway, facilitate the redox

1 reactions and improve the durability. Metal layered double hydroxides (LDHs) with
2 hydrotalcite-like structure and pseudo-capacitivity have drawn many attentions as
3 supercapacitors, due to their excellent anion exchanging capability and remarkable
4 intercalating ability [36-38]. Therefore, appropriately integrating metal phosphides
5 with hydroxides is promised to be a superior electrode material for supercapacitors,
6 which is expected to enhance the capacitance and improve the cycle stability.

7 Inspired by the aspects mentioned above, we fabricated hierarchical
8 $\text{Ni}_2\text{P}@ \text{Ni}(\text{OH})_2$ architecture grown on carbon cloth (CC) through a combined
9 phosphorization and hydrothermal route. $\text{Ni}_2\text{P}@ \text{Ni}(\text{OH})_2@ \text{CC}$ is directly used as
10 a binder-free battery-type electrode for hybrid supercapacitors. In addition to the
11 synergistic effects of combined advantages for Ni_2P and $\text{Ni}(\text{OH})_2$ as mentioned above,
12 the $\text{Ni}_2\text{P}@ \text{Ni}(\text{OH})_2@ \text{CC}$ electrode is also promised to possess multiple advantages.
13 First, the $\text{Ni}_2\text{P}@ \text{Ni}(\text{OH})_2$ composites show three-dimensional hierarchical
14 architectures, in which both the Ni_2P and $\text{Ni}(\text{OH})_2$ components show ultrathin
15 nanosheet structures. The special hierarchical structure is supposed to have large
16 surface area and rich electro-active sites, which make the contact between electrode
17 materials and electrolyte more sufficient. Second, as a cheap conductive textile,
18 carbon cloth is used as flexible substrate and current collector, which possesses
19 desirable features such as low cost, chemical stability, high conductivity and excellent
20 mechanical flexibility. Third, hierarchical $\text{Ni}_2\text{P}@ \text{Ni}(\text{OH})_2$ architectures were directly
21 grown on the flexible conductive carbon cloth substrate without using organic binders,
22 which can reduce the resistance between electrode materials and substrate, promoting

1 the charge transfer. These benefits make the $\text{Ni}_2\text{P@Ni(OH)}_2\text{@CC}$ electrode a
2 promised candidate for supercapacitors.

3 **2 Experiment details**

4 **2.1 Reagents**

5 $\text{NiCl}_2\cdot 6\text{H}_2\text{O}$ was obtained from Tianjin kwangfu Fine Chemical Industry Research
6 Institute. Tetramethothylamine (HMT), $\text{NaH}_2\text{PO}_2\cdot\text{H}_2\text{O}$ and potassium hydroxide
7 (KOH) were purchased from Sinopharm Chemical Reagents Co., Ltd., China. Before
8 experiment, the carbon cloth (CC) with a size of 1 cm \times 2 cm was successively
9 cleaned by ultrasonication in ethanol and deionized water for each 30 min, and finally
10 dried at 60 °C for 8 h under vacuum conditions.

11 **2.2 Synthesis of hierarchical Ni(OH)_2 nanoarray precursor on CC**

12 Ni(OH)_2 nanosheet arrays were directly grown on CC by a simple hydrothermal route.
13 $\text{NiCl}_2\cdot 6\text{H}_2\text{O}$ (4 mmol) and HMT (1.6 g) were dissolved into de-ionized water (60 ml)
14 under magnetic stirring. Then, the above solution was poured into a Teflon-lined
15 stainless-steel autoclave (100 mL), and several pieces of CC were immersed into the
16 above solution. The autoclave was sealed and then heated at 100 °C for 6 h in an
17 electric oven. After the reaction was finished, the $\text{Ni(OH)}_2\text{@CC}$ electrode was rinsed
18 with de-ionized water and ethanol, and dried at 60 °C.

19 **2.3 Synthesis of hierarchical $\text{Ni}_2\text{P@CC}$**

20 $\text{Ni}_2\text{P@CC}$ was fabricated by phosphorization route using $\text{Ni(OH)}_2\text{@CC}$ as precursor.
21 Typically, the prepared $\text{Ni(OH)}_2\text{@CC}$ and $\text{NaH}_2\text{PO}_2\cdot\text{H}_2\text{O}$ were put at two separated
22 positions in a quartz boat with $\text{NaH}_2\text{PO}_2\cdot\text{H}_2\text{O}$ at the upstream side of the tube furnace.

1 The tube furnace was heated to 300 °C with a heating rate of 2 °C/min and kept at
2 300 °C for 2 h. During all the processes, the furnace was protected in Ar atmosphere.

3 **2.4 Synthesis of Ni₂P@Ni(OH)₂@CC**

4 Ni₂P@Ni(OH)₂@CC was fabricated by a second hydrothermal route. The detailed
5 processes were consistent with the preparation method of Ni(OH)₂@CC precursor.

6 Ni₂P@CC was immersed into the solution instead of CC, which was used as the
7 substrate. Besides, the autoclave was kept at 100 °C for 90 min.

8 **2.5 Characterization**

9 The structures of samples were determined by X-ray diffraction (XRD) using Cu K_α
10 radiation (DX-2700, λ = 1.5418 Å) in the 2θ range of 10-80° with a step size of 0.02°.

11 The morphologies were characterized by scanning electron microscopy (FESEM,
12 Hitachi S-4800 microscope) and transmission electron microscopy TEM (FEI Tecnai
13 G² F20). The elemental compositions were tested by X-ray photoelectron
14 spectroscopy (XPS, ESCALAB210) and Energy dispersive spectroscopy (EDS)
15 equipped in SEM. The Ni contents of active material were determined by inductively
16 coupled plasma emission spectrometer (ICP-MS, 720-ES, VARIAN).

17 **2.6 Electrochemical measurements**

18 Electrochemical analyses were performed on a CHI 760E electrochemical workstation
19 (Shanghai CH Instrument Company). Cyclic voltammetry (CV), galvanostatic
20 charge-discharge (GCD) and electrochemical impedance spectroscopy (EIS) of the
21 samples were carried out in a three-electrode setup using 6 M KOH aqueous solution
22 as the electrolyte. The fabricated electrodes, standard calomel electrode (SCE) and Pt

1 electrode were used as working electrode, reference electrode and counter electrode,
2 respectively.

3 The specific capacitance is calculated from the GCD curves according to the
4 following equations [39, 40]:

$$5 \quad C_m = I\Delta t / m \quad (1)$$

$$6 \quad C_s = I\Delta t / s \quad (2)$$

7 where C_m is the gravimetric capacitance ($C \text{ g}^{-1}$), C_s is the areal capacitance ($C \text{ cm}^{-2}$), I
8 is the discharge current (A), Δt represents the discharging time (s), and m and s
9 designate the mass of active material (g) and geometrical area (cm^2), respectively.

10 **2.7 Assembly of the hybrid supercapacitor device**

11 The hybrid supercapacitor (HSC) was assembled using $\text{Ni}_2\text{P@Ni(OH)}_2\text{@CC}$ as the
12 positive electrode and active carbon as the negative electrode. The HSC was packaged
13 in a 2032-type button cell, in which a polypropylene membrane was used to separate
14 the two electrodes. The negative electrode was fabricated by mixing activated carbon
15 (AC), acetylene black and polytetrafluoroethylene (PTFE) with a weight ratio of 8: 1:
16 1. The forming slurry was painted on CC substrate and then dried at $60 \text{ }^\circ\text{C}$ in a
17 vacuum oven for 12 h. Generally, the positive and negative electrodes in the HSC
18 device should satisfy charge balance principle ($q^+ = q^-$). The mass of AC can be
19 obtained by the following equations [21]:

$$20 \quad q = C_m \times m \times \Delta V \quad (3)$$

$$21 \quad \frac{m_+}{m_-} = \frac{C_m^- \times \Delta V^-}{C_m^+ \times \Delta V^+} \quad (4)$$

22 where m is the weight of active material, C_m is the specific capacity and ΔV is the

1 potential window of electrode. The superscripts of '+' and '-' present the positive and
2 negative electrodes, respectively.

3 The energy density (E) and power density (P) can be calculated by the following
4 equations [41]:

$$5 \quad E = I \int V(t) dt / m \quad (5)$$

$$6 \quad P = E / \Delta t \quad (6)$$

7 **3 Results and discussions**

8 [Fig. 1](#) shows the possible formation mechanism of hierarchical Ni₂P@Ni(OH)₂@CC
9 electrode. Firstly, the hierarchical Ni(OH)₂ nanoarray precursor was in-situ grown on
10 flexible carbon cloth (CC) at a low temperature of 100 °C through a facile
11 hydrothermal method. Then, the Ni(OH)₂@CC precursor was treated at 300 °C by a
12 phosphorization route using NaH₂PO₂·H₂O as the phosphorus source, forming
13 Ni₂P@CC. Finally, Ni₂P@CC was treated by a secondary hydrothermal route,
14 resulting in the formation of Ni₂P@Ni(OH)₂@CC electrode. [Fig. S1a](#) shows the XRD
15 pattern of Ni₂P@Ni(OH)₂@CC. Only the diffraction peaks of Ni₂P (JCPDS: 74-1385)
16 are obtained. The additional diffraction peak at about 26° belongs to carbon (JCPDS:
17 38-0715) from the CC substrate. No diffraction peaks of Ni(OH)₂ are found. This is
18 mainly due to the combined effects of low crystallinity of hydroxides and tiny amount
19 of Ni(OH)₂ on the CC substrate (The mass loadings of Ni₂P and Ni₂P@Ni(OH)₂ on
20 CC substrate are 0.85 and 1.15 mg cm⁻², respectively.). To further examine the
21 crystalline phases of active materials in the electrodes, the corresponding
22 nanopowders which were fabricated by the same process are also analyzed by XRD

1 technology, as shown in Fig. S1b. The diffraction peaks of precursor (red line) can be
2 well indexed into α -Ni(OH)₂ with layered hydroxide structure. The broad diffraction
3 peaks suggest that the α -Ni(OH)₂ component has a low crystallinity. After
4 phosphorization treatment, the diffraction peaks (black line) can be assigned to Ni₂P
5 with hexagonal phase. The XRD patterns of nanopowders further demonstrate the
6 success of phosphorization treatment.

7 Fig. 2a shows the optical photographs of CC substrate, Ni(OH)₂@CC, Ni₂P@CC
8 and Ni₂P@Ni(OH)₂@CC. Obviously, the color of the slices changes after each
9 preparation process, suggesting that the active materials were successfully in-situ
10 grown on the CC substrate as we desired. Optical photograph in Fig. 2b shows that
11 the Ni₂P@Ni(OH)₂@CC electrode is flexible, which is of great significance for the
12 practical applications of supercapacitors. The morphologies and microstructures of the
13 electrodes were characterized by SEM and TEM. The CC substrate is weaved by
14 crossed carbon microfibers (Fig. S2). After in-situ growth, the active materials with
15 high density are densely packed on the microfibers of CC substrate (Fig. 2c and Fig.
16 S2b-c). From the high-magnification SEM image (Inset of Fig. 2c), the
17 Ni₂P@Ni(OH)₂ shows a three-dimensional (3D) hierarchical architecture which is
18 assembled by uninterrupted ultrathin nanosheets. The interconnected nanosheets of
19 Ni₂P and Ni(OH)₂ result in the formation of 3D network structure with multi-porous
20 surface, which is promised to provide high specific surface area and abundant open
21 space. This unique structure can provide numerous electroactive sites and fast ionic
22 diffusion pathway, which are beneficial for their electrochemical behaviors. EDS

1 spectrum of Ni₂P@Ni(OH)₂@CC (Fig. S3) contains C, O, P and Ni elements, which
2 is consistent with the XRD results. The EDS elemental mappings of
3 Ni₂P@Ni(OH)₂@CC (Fig. 2d) further confirm that the Ni, P and O elements are
4 uniformly distributed throughout the whole CC microfiber. Compared to the mapping
5 of P element, the mappings of Ni and O elements show relative larger distribution
6 areas, suggesting that Ni(OH)₂ nanosheets successfully cover on the surface of Ni₂P
7 after the second hydrothermal route. ICP data (Table S1) reveals that the ratio of Ni
8 and P in Ni₂P@Ni(OH)₂@CC is greater than 2:1, further confirming that the desired
9 phase has been successfully formed. For TEM characterization, the active materials
10 were scraped off from the CC substrate. Fig. 2e-f show the representative TEM
11 images of Ni₂P@Ni(OH)₂. HRTEM image in Fig. 2f shows interplanar spacing
12 distances of 0.204 and 0.233 nm, corresponding to the (201) crystalline plane of Ni₂P
13 and (015) crystalline plane of Ni(OH)₂, respectively.

14 The surface chemical constitutions and electronic states of Ni₂P@CC and
15 Ni₂P@Ni(OH)₂@CC electrodes were characterized by XPS. Full scan XPS spectrum
16 of Ni₂P@Ni(OH)₂@CC (Fig. S4) indicates the existence of C, O, Ni and P elements
17 in the electrodes. Fig. 3a shows the high-resolution Ni 2p XPS spectra of Ni₂P@CC
18 and Ni₂P@Ni(OH)₂@CC electrodes. For the Ni₂P@CC (the down line in Fig. 3a), the
19 spectrum shows two spin-orbit doublets peaks at 857.6 and 875.2 eV, corresponding
20 to the Ni 2p_{3/2} and Ni 2p_{1/2} of Ni²⁺, respectively. Besides, two obvious shakeup peaks
21 at 862.5 and 880.6 eV are related to the Ni 2p_{3/2} satellite and Ni 2p_{1/2} satellite,
22 respectively. The peaks at 853.0 eV is probably attributed to the metallic Ni with

1 binding energy of 852.6 eV, which is due to the partially charged Ni species ($\text{Ni}^{\delta+}$, δ is
2 closed to 0) [42]. The high-resolution XPS spectrum of Ni 2p of $\text{Ni}_2\text{P}@(\text{OH})_2@\text{CC}$
3 (top line in Fig. 3a) consists of two spin-orbit doublets accompanied by
4 two shakeup satellites. The doublet fitting peaks with binding energies at 857.1 and
5 874.8 eV correspond to the Ni $2p_{3/2}$ and Ni $2p_{1/2}$ of Ni^{2+} , respectively. The other two
6 peaks are two plump shake-up satellite peaks (denoted as “Sat.”) of Ni^{2+} [43].
7 Compared to $\text{Ni}_2\text{P}@\text{CC}$, the Ni $2p_{3/2}$ peak of $\text{Ni}_2\text{P}@(\text{OH})_2@\text{CC}$ shifts to lower
8 binding energy with a difference of 0.5 eV. High-resolution P 2p XPS spectra (Fig. 3b)
9 shows that the P 2p peaks in $\text{Ni}_2\text{P}@\text{CC}$ and $\text{Ni}_2\text{P}@(\text{OH})_2@\text{CC}$ are 134.7 and 133.6
10 eV, respectively, corresponding to the typical of phosphate species, which is mainly
11 due to the partial superficial passivation of P species [44]. Obviously, the P 2p peak in
12 $\text{Ni}_2\text{P}@(\text{OH})_2@\text{CC}$ also shifts to lower binding energy with a big difference of 1.1
13 eV, which is probably due to the improved electron cloud density around the P atoms
14 by the introduction of $\text{Ni}(\text{OH})_2$. These obvious shift phenomenons of Ni 2p and P 2p
15 indicate the possible existence of strong electronic interactions and electron transfer at
16 the interface between Ni_2P and $\text{Ni}(\text{OH})_2$ [45]. The strong electronic interaction can
17 generate internal electric fields, resulting in the improvement of electronic
18 conductivity at the interfaces [34]. These results suggest that the in-situ growth of
19 $\text{Ni}(\text{OH})_2$ may greatly affect the electrochemical performance of Ni_2P .

20 Fig. 4a shows the CV curves of $\text{Ni}_2\text{P}@\text{CC}$ and $\text{Ni}_2\text{P}@(\text{OH})_2@\text{CC}$ electrodes at a
21 sweep rate of 5 mV s^{-1} . Fig. 4b reveals the GCD curves of the two electrodes
22 measured at a current density of 1 mA cm^{-2} . The CV and GCD measurements for the

1 two electrodes are carried out within a potential window from -0.2 to 0.6 V. Both the
2 Ni₂P@CC and Ni₂P@Ni(OH)₂@CC electrodes exhibit broad redox reaction peaks
3 with noticeable faradaic current (Fig. 4a) and clearly potential platform (Fig. 4b),
4 indicating a representative battery-type pseudocapacitive feature [46, 47]. Obviously,
5 the covering area of CV curve and discharge time of GCD curve for the
6 Ni₂P@Ni(OH)₂@CC electrode is far higher than those of Ni₂P@CC electrode, which
7 directly indicates that the second growth of Ni(OH)₂ can greatly increase the specific
8 capacitance and electrochemical performance of Ni₂P. Fig. 4c shows the typical CV
9 curves of Ni₂P@Ni(OH)₂@CC electrode measured at different sweep rates ranging
10 from 5 to 50 mV s⁻¹. Two distinct redox peaks can be observed, which are related to
11 the reversible electrochemical reactions of Ni²⁺ in the electrolyte. By increasing the
12 scanning rates from 5 to 50 mV s⁻¹, the redox current increases gradually and the
13 redox peaks shift to lower potential, which are mainly attributed to the charge
14 diffusion polarization during the charging process [48, 49]. Fig. 4d reveals the GCD
15 curves of Ni₂P@Ni(OH)₂@CC electrode measured at various current densities
16 ranging from 1 to 10 mA cm⁻². All the GCD curves present clearly potential platform,
17 which further indicates the outstanding battery-type pseudocapacitive characteristics.
18 Compared with Ni₂P@CC (Fig. S5), the GCD curves of Ni₂P@Ni(OH)₂@CC
19 electrode at different current densities show more symmetric potential-time shape,
20 suggesting that the Ni₂P@Ni(OH)₂@CC electrode shows higher charge/discharge
21 coulombic efficiency with lower electric polarization. Fig. 4e shows the comparison
22 of areal capacitances and gravimetric capacitances between Ni₂P@CC and

1 Ni₂P@Ni(OH)₂@CC electrodes at various current densities, which were calculated
2 from the GCD curves according to the equations (1) and (2). Noteworthy, compared
3 to Ni₂P@CC, the Ni₂P@Ni(OH)₂@CC electrode has higher areal capacitances and
4 gravimetric capacitances in the whole current densities. At a low current density of 1
5 mA cm⁻², the Ni₂P@Ni(OH)₂@CC electrode has a gravimetric capacitance of 632 C
6 g⁻¹ and areal capacitance of 0.73 C cm⁻², which are 2 and 2.7 times larger than those
7 of Ni₂P@CC (321 C g⁻¹ and 0.27 C cm⁻²), respectively. At a high current density of 10
8 mA cm⁻², the gravimetric capacitances of Ni₂P@Ni(OH)₂@CC and Ni₂P@CC
9 electrodes are 400 and 138 C g⁻¹, respectively. The Ni₂P@Ni(OH)₂@CC electrode has
10 an improved rate capability of 63.3 %, while the rate capability of Ni₂P@CC is only
11 42.9 %.

12 Electrochemical impedance spectra (EIS) is used to evaluate the ions migration rate
13 on the surface of electrodes, and the transport kinetics of charge diffusion, which is
14 carried out at an open circuit potential in the frequency ranging from 0.01 Hz to 100
15 kHz. Fig. 4f shows the Nyquist impedance plot of Ni₂P@CC and
16 Ni₂P@Ni(OH)₂@CC electrodes. The real axis intercept at the high frequency range
17 represents ohmic series impedance (R_s), which reflects the ionic resistance of
18 electrolyte, inherent resistances of electrodes and interface resistance [50]. And we
19 also use the R_s to reflect the conductivity of the materials [51, 52]. R_s of
20 Ni₂P@Ni(OH)₂@CC electrode (0.9168 Ω) was decreased in comparison with that of
21 Ni₂P@CC (1.077 Ω). This suggests that Ni₂P@Ni(OH)₂@CC has better electron
22 conductivity and excellent pathways for electron transport [45], which is desirable for

1 high power density. The result is accordant with the CV and GCD results, which
2 indicates that Ni₂P@Ni(OH)₂@CC has much better electrochemical performance than
3 Ni₂P@CC.

4 In order to investigate the charge storage mechanism of Ni₂P@CC and
5 Ni₂P@Ni(OH)₂@CC electrodes, the corresponding CV results were further analyzed
6 (Fig. S6 and Fig. 4c). Generally, the relationship between measured current (*i*) and
7 scan rate (*v*) obeys the power law [53-56]:

$$8 \quad i = av^b \quad (7)$$

9 where both *a* and *b* are constants. In the case of diffusion-controlled and surface
10 capacitive processes, *b* value approaches 0.5 and 1, respectively. Fig. 5 shows the
11 fitting results of *b* value using anodic peaks. The *b* values of Ni₂P@CC and
12 Ni₂P@Ni(OH)₂@CC are calculated to be 0.50 and 0.62, respectively. This result
13 suggests that diffusion process is the major factors that determine the electrochemical
14 properties of Ni₂P and Ni₂P@Ni(OH)₂. Compared to Ni₂P, the introduction of
15 Ni(OH)₂ can improve the surface capacitive ability of Ni₂P@Ni(OH)₂.

16 Cycling stability is another important criterion in the supercapacitor applications, as
17 shown in Fig. 6. The capacitive retention of Ni₂P@Ni(OH)₂@CC electrode was
18 approximately 81.4% after 1000 charge/discharge cycles at a constant current density
19 of 2 mA cm⁻², much higher than that of Ni₂P@CC (51.8%). Compared to Ni₂P@CC
20 electrode, the capacitive retention of the Ni₂P@Ni(OH)₂@CC electrode increases in
21 the early cycles and keeps unchanged, indicating that this electrode material has a
22 good cycling stability. The initial increase in specific capacity could be ascribed to the

1 infiltration and activation of Ni₂P@Ni(OH)₂@CC electrode, which is also present in
2 other phosphide materials [57]. Besides, the Ni₂P@Ni(OH)₂@CC electrode exhibits
3 over 95% of coulombic efficiency after 1000 charge-discharge cycles, demonstrating
4 good stability (Fig. S7). And the SEM image of Ni₂P@Ni(OH)₂@CC electrode after
5 electrochemical testing is shown in the Fig. S8. Its morphology can still maintain the
6 multistage nanosheets structure, indicating that the electrode material has good
7 structural stability. The good cycling stability is mainly due to the unique
8 three-dimensional hierarchical architecture with self-assembled uninterrupted
9 ultrathin nanosheets on the surface of the material.

10 To further investigate the potential applications of the electrode, a hybrid
11 supercapacitors (HSC) device was assembled by employing Ni₂P@Ni(OH)₂@CC as
12 the anode and AC as the cathode. To satisfy the charge balance, the mass of AC was
13 calculated using the equations (3) and (4). Fig. 7a reveals the CV curves of the HSC
14 device measured at different scan rates, which show a potential window of 0-1.6 V.
15 GCD curves of the HSC device are displayed in Fig. 7b. A clearly potential platform
16 can be seen in all the GCD curves measured at different current densities, suggesting
17 that the device should possess both electrical double-layer capacity and battery-like
18 capacity. Fig. 7c shows the corresponding specific capacitances obtained from Fig. 7b.
19 The specific capacitances are 247.4 and 119.8 mC cm⁻² at 1 and 10 mA cm⁻²,
20 respectively. The energy density and power density of the Ni₂P@Ni(OH)₂@CC//AC
21 HSC device were calculated by the equations (5) and (6). Fig. 7d shows the Ragone
22 plots of energy densities and power densities obtained from the GCD curves. The

1 maximum energy density reaches 23.5 Wh kg^{-1} at a power density of 1158.0 W kg^{-1} ,
2 and remains 12.5 Wh kg^{-1} at 3756.3 W kg^{-1} . Table S2 shows the comparison of energy
3 densities and power densities of $\text{Ni}_2\text{P@Ni(OH)}_2\text{/CC//AC}$ device with other Ni-based
4 phosphides HSC devices. Obviously, the $\text{Ni}_2\text{P@Ni(OH)}_2\text{/CC//AC}$ device represents
5 comparable or even better energy densities. Fig. 7e displays the cycling stability
6 performance of $\text{Ni}_2\text{P@Ni(OH)}_2\text{/CC//AC}$ HSC device. The charge/discharge cycles
7 were operated at 5 mA cm^{-2} for 5000 cycles. The $\text{Ni}_2\text{P@Ni(OH)}_2\text{/CC//AC}$ HSC
8 device reveal good cycling stability, which possesses 75.2% maintenance after 5000
9 cycles.

10 **4 Conclusions**

11 In summary, three-dimensional hierarchical $\text{Ni}_2\text{P@Ni(OH)}_2$ architecture was in-situ
12 grown on a flexible carbon cloth substrate, which was used as a novel binder-free
13 hybrid-type electrode for supercapacitor applications. Taking the combined benefits of
14 high electronic conductivity of Ni_2P , superior anion exchanging/intercalating capacity
15 of Ni(OH)_2 , special 3D porous hierarchical architectures and excellent flexibility of
16 carbon cloth, the $\text{Ni}_2\text{P@Ni(OH)}_2\text{/CC}$ electrode shows boosting specific capacitance,
17 rate capability and charge/discharge cycle stability in comparison with $\text{Ni}_2\text{P/CC}$.
18 Charge storage mechanism investigations show that the introduction of Ni(OH)_2 can
19 improve the surface capacitive ability of Ni_2P . The assemble
20 $\text{Ni}_2\text{P@Ni(OH)}_2\text{/CC//AC}$ hybrid supercapacitor device shows high energy density
21 and good cycling stability. This study demonstrates that the three-dimensional
22 hierarchical $\text{Ni}_2\text{P@Ni(OH)}_2\text{/CC}$ architecture with advanced synergistic effects holds

1 great promise as hybrid electrode for supercapacitors.

2 **Acknowledgements**

3 This work was supported by the National Natural Science Foundation of China
4 (51572218), Natural Science Foundation of Shaanxi Province (2017KCT-01,
5 2019JM-138), Scientific Research Program Funded by Shaanxi Provincial Education
6 Department (18JK0786), Young Talent Fund of University Association for Science
7 and Technology in Shaanxi (20170605) and Key Project of Research and
8 Development of Shaanxi Province (2018ZDCXL-GY-08-05).

9 **Compliance with ethical standards**

10 **Conflict of interest** The authors declare no conflicts of interest.

11 **References**

- 12 1. J.T. Zhang, X.S. Zhao, On the configuration of supercapacitors for maximizing
13 electrochemical performance. *ChemSusChem* **5**, 818-841 (2012).
- 14 2. X.R. Li, J.L. Wei, Q. Li, S.S. Zheng, Y.X. Xu, P. Du, C.Y. Chen, J.J. Zhao, H.G.
15 Xue, Q. Xu, H. Pang, Nitrogen-doped cobalt oxide nanostructures derived from
16 cobalt-alanine complexes for high-performance oxygen evolution reactions. *Adv.*
17 *Funct. Mater.* **28**, 1800886 (2018).
- 18 3. Y.H. Feng, S.H. Chen, J. Wang, B.A. Lu, Carbon foam with microporous structure
19 for high performance symmetric potassium dual-ion capacitor. *J. Energy Chem.*
20 **43**, 129-138 (2020).
- 21 4. X.R. Li, X.C. Yang, H.G. Xue, H. Pang, Q. Xu, Metal-organic frameworks as a
22 platform for clean energy applications. *EnergyChem.* **2**, 100027 (2020).

- 1 5. X.Z. Yu, B.A. Lu, Z. Xu, Super Long-life supercapacitors based on the construction
2 of nanohoneycomb-like strongly coupled CoMoO₄-3D graphene hybrid electrodes.
3 Adv. Mater. **26**, 1044-1051 (2014).
- 4 6. P. Poizot, F. Dolhem, Clean energy new deal for a sustainable world: from non-CO₂
5 generating energy sources to greener electrochemical storage devices. Energy
6 Environ. Sci. **4**, 2003 (2011).
- 7 7. B.W. He, P.Y. Kuang, X.H. Li, H. Chen, J.G. Yu, K. Fan, In situ transformation of
8 prussian-blue analogue-derived bimetallic carbide nanocubes by water oxidation:
9 applications for energy storage and conversion. Chem. Eur. J. **25**, 1-12 (2019).
- 10 8. G.P. Wang, L. Zhang, J.J. Zhang, A review of electrode materials for
11 electrochemical supercapacitors. Chem. Soc. Rev. **41**, 797-828 (2012)
- 12 9. C. Peng, S.W. Zhang, X.H. Zhou, G.Z. Chen, Unequalisation of electrode
13 capacitances for enhanced energy capacity in asymmetrical supercapacitors.
14 Energy Environ. Sci. **3**, 1499-1502 (2010).
- 15 10. G.Q. Zhang, H.B. Wu, H.E. Hoster, M.B. Chan-Park, X.W. (David) Lou,
16 Single-crystalline NiCo₂O₄ nanoneedle arrays grown on conductive substrates as
17 binder-free electrodes for high-performance supercapacitors. Energy Environ.
18 Sci. **5**, 9453-9456 (2012).
- 19 11. J.R. Miller, P. Simon, Electrochemical capacitors for energy management. Science
20 **321**, 651-652 (2008).
- 21 12. W. Zhou, K. Yu, D. Wang, J. Chu, J. Li, L. Zhao, C. Ding, Y. Du, X. Jia, H. Wang,
22 G. Wen, Hierarchically constructed NiCo₂S₄@Ni_(1-x)Co_x(OH)₂ core/shell

- 1 nanoarrays and their application in energy storage. *Nanotechnol.* **27**, 235402
2 (2016).
- 3 13. S. Peng, L. Li, H. B. Wu, S. Madhavi, X. W. (David) Lou, Controlled growth of
4 NiMoO₄ nanosheet and nanorod arrays on various conductive substrates as
5 advanced electrodes for asymmetric supercapacitors. *Adv. Energy Mater.* **5**,
6 1401172 (2015).
- 7 14. T. Liu, L.Y. Zhang, W. You, J.G. Yu, Core-shell nitrogen-doped carbon hollow
8 spheres/Co₃O₄ nanosheets as advanced electrode for high-performance
9 supercapacitor. *Small* **14**, 1702407 (2018).
- 10 15. Y. Zhong, X. Xia, F. Shi, J. Zhan, J. Tu, H.J. Fan, Transition metal carbides and
11 nitrides in energy storage and conversion. *Adv. Sci.* **3**, 1500286 (2016).
- 12 16. E. Frackowiak, Carbon materials for supercapacitor application, *Phys. Chem.*
13 *Chem. Phys.* **9**, 1774-1785 (2007).
- 14 17. Y. Wang, Y. Xia, Recent progress in supercapacitors: from materials design to
15 system construction. *Adv. Mater.* **25**, 5336-5342 (2013).
- 16 18. P. Simon, Y. Gogotsi, Materials for electrochemical capacitors. *Nat. Mater.* **7**,
17 845-854 (2008).
- 18 19. Y.Z. Hu, C.H. Huang, S.P Jiang, Y.L. Qin, H. Chen, Hierarchical nickel-cobalt
19 selenide nanoparticles/nanosheets as advanced electroactive battery materials for
20 hybrid supercapacitors. *J. Colloid Interface Sci.* **558**, 291-300 (2020).
- 21 20. W.L. Hong, L.Y. Lin, Design of nickel cobalt oxide and nickel cobalt
22 oxide@nickel molybdenum oxide battery-type materials for flexible solid-state

- 1 battery supercapacitor hybrids. *J. Power Sources* **435**, 226797 (2019).
- 2 21. Y.M. Hu, M.C. Liu, Y.X. Hu, Q.Q. Yang, L.B. Kong, L. Kang, One-pot
3 hydrothermal synthesis of porous nickel cobalt phosphides with high
4 conductivity for advanced energy conversion and storage. *Electrochim. Acta* **215**,
5 114-125 (2016).
- 6 22. J. Wen, S.Z. Li, T. Chen, B. Li, L.B. Xiong, Y.X. Guo, G.J. Fang, Porous
7 nanosheet network architecture of CoP@Ni(OH)₂ composites for high
8 performance supercapacitors. *Electrochim. Acta* **258**, 266-273 (2017)
- 9 23. X. Li, H. Wu, A.M. Elshahawy, L. Wang, S.J. Pennycook, C. Guan, J. Wang,
10 Cactus-like NiCoP/NiCo-OH 3D architecture with tunable composition for
11 high-performance electrochemical capacitors. *Adv. Funct. Mater.* **28**, 1800036
12 (2018).
- 13 24. S. Wang, Z. Xiao, S. Zhai, G. Wang, Q. An, D. Yang, A high-temperature
14 phosphorization for synthesis of core-shell Ni-Ni_xP_y@C nanocomposite-
15 immobilized sponge-like P-doped porous carbon with excellent supercapacitance
16 performance. *Electrochim. Acta* **309**, 197-208 (2019).
- 17 25. Y. Xu, S. Hou, G. Yang, X. Wang, T. Lu, L. Pan, Synthesis of bimetallic Ni_xCo_{1-x}P
18 hollow nanocages from metal-organic frameworks for high performance hybrid
19 supercapacitors. *Electrochim. Acta* **285**, 192-201 (2018).
- 20 26. X. Li, A. MEIshahawy, C. Guan, J. Wang, Metal phosphides and phosphates-based
21 electrodes for electrochemical supercapacitors. *Small* **13**, 1701530 (2017).
- 22 27. D. Wang, L.B. Kong, M.C. Liu, W.B. Zhang, Y.C. Luo, L. Kang, Amorphous Ni-P

- 1 materials for high performance pseudocapacitors. *J. Power Sources* **274**,
2 1107-1113 (2015).
- 3 28. H. Wu, Y.H. Ni, M.F. Wang, D.C. Lu, Shape-controlled synthesis and performance
4 comparison of Ni₂P nanostructures. *CrystEngComm* **18**, 5155-5163 (2016).
- 5 29. J.L. Xing, J. Du, X. Zhang, Y.B. Shao, T. Zhang, C.L. Xu, A Ni-P@NiCo LDH
6 core-shell nanorod-decorated nickel foam with enhanced areal specific
7 capacitance for high-performance supercapacitors. *Dalton Trans.* **46**, 10064
8 (2017).
- 9 30. Y. Cheng, Y.F. Zhang, H.M. Jiang, X.Y. Dong, J.Q. Zheng, C.G. Meng,
10 Synthesis of amorphous cobalt silicate nanobelts@manganese silicate core-shell
11 structures as enhanced electrode for high-performance hybrid supercapacitors. *J.*
12 *Colloid Interface Sci.* **561**, 762-771 (2020).
- 13 31. M. Racik K, A. Manikandan, M. Mahendiran, J. Madhavana, M.V. Antony Raj,
14 M.G. Mohamed, T. Maiyalagan, Hydrothermal synthesis and characterization
15 studies of α -Fe₂O₃/MnO₂ nanocomposites for energy storage supercapacitor
16 application. *Ceram. Int.* **46**, 6222-6233 (2020).
- 17 32. Y.H. Tian, L.Y. Lin, M.L. Ning, S. Hussain, H. Su, M.S. Javed, H.J. Zhen, N. Hu,
18 A. Shaheen, Novel binder-free electrode of NiCo₂O₄@NiMn₂O₄ core-shell
19 arrays modified carbon fabric for enhanced electrochemical properties. *Ceram.*
20 *Int.* **45**, 16904-16910 (2019).
- 21 33. T.F. Yi, J. Mei, B.L. Guan, P. Cui, S.H. Luo, Y. Xie, Y.G. Liu, Construction of
22 spherical NiO@MnO₂ with core-shell structure obtained by depositing MnO₂

- 1 nanoparticles on NiO nanosheets for high-performance supercapacitor. *Ceram.*
2 *Int.* **46**, 421-429 (2020).
- 3 34. X. Gao, Y. Zhao, K. Dai, J. Wang, B. Zhang, X. Shen, NiCoP
4 nanowire@NiCo-layered double hydroxides nanosheet heterostructure for
5 flexible asymmetric supercapacitors. *Chem. Eng. J.* **384**, 123373 (2020).
- 6 35. Z. Ma, F. Jing, Y. Fan, L. Hou, L. Su, L. Fan, G. Shao, High-stability MnO_x
7 nanowires@C@MnO_x nanosheet core-shell heterostructure pseudocapacitance
8 electrode based on reversible phase transition mechanism. *Small* **15**, 1900862
9 (2019).
- 10 36. J. Yang, C. Yu, X. Fan, J. Qiu, 3D Architecture materials made of NiCoAl-LDH
11 nanoplates coupled with NiCo-carbonate hydroxide nanowires grown on flexible
12 graphite paper for asymmetric supercapacitors. *Adv. Energy Mater.* **4**,
13 1400761-1400769 (2014).
- 14 37. Z. Lu, W. Zhu, X. Lei, G.R. Williams, D. O'Hare, Z. Chang, X. Sun, X. Duan,
15 High pseudocapacitive cobalt carbonate hydroxide films derived from CoAl
16 layered double hydroxides. *Nanoscale* **4**, 3640-3643 (2012).
- 17 38. S.C. Sekhar, G. Nagaraju, J.S. Yu, Conductive silver nanowires-fenced carbon
18 cloth fibers-supported layered double hydroxide nanosheets as a flexible and
19 binder-free electrode for high-performance asymmetric supercapacitors. *Nano*
20 *Energy* **36**, 58-67 (2017).
- 21 39. D.D. Wei, Y.L. Zhang, X.Z. Zhu, M.L. Fan, Y.L. Wang, CNT/Co₃S₄@NiCo LDH
22 ternary nanocomposites as battery-type electrode materials for hybrid

- 1 supercapacitors. *J. Alloy. Compd.* **824**, 153937 (2019).
- 2 40. J. Wang, Q. Zhong, Y.Q. Zeng, D.Y. Cheng, Y.G. Xiong, Y.F. Bu, Rational
3 construction of triangle-like nickel-cobalt bimetallic metal-organic framework
4 nanosheets arrays as battery-type electrodes for hybrid supercapacitors. *J.*
5 *Colloid Interface Sci.* **555**, 42-52 (2019).
- 6 41. H.C. Chen, S.P. Jiang, B.H. Xu, C.H. Huang, Y.Z. Hu, Y.L. Qin, M.X. He, H.J.
7 Cao, Sea-urchin-like nickel-cobalt phosphide/phosphate composites as advanced
8 battery materials for hybrid supercapacitors. *J. Mater. Chem. A* **7**, 6241 (2019).
- 9 42. C.X. Zhou, T.T. Gao, Y.J. Wang, Q.L. Liu, D. Xiao, Through a hydrothermal
10 phosphatization method synthesized NiCo and Fe based electrodes for
11 high-performance battery-supercapacitor hybrid device. *Appl. Surf. Sci.* **475**,
12 729-739 (2019).
- 13 43. B.B. Cheng, W. Zhang, M. Yang, Y.J. Zhang, F.B. Meng, Preparation and study of
14 porous MnCo₂O₄@NiO nanosheets for high-performance supercapacitor. *Ceram.*
15 *Int.* **45**, 20451-20457 (2019).
- 16 44. X.J. Zhang, S.J. Hou, Z.B. Ding, G. Zhu, H.R. Tang, Y.C. Hou, T. Lu, L.K. Pan,
17 Carbon wrapped CoP hollow spheres for high performance hybrid supercapacitor.
18 *J. Alloy. Compd.* **822**, 153578 (2019).
- 19 45. H.J. Zhang, X.P. Li, A. Hähnel, V. Naumann, C. Lin, S. Azimi, S.L. Schweizer, A.
20 W. Maijenburg, R. B. Wehrspohn, Bifunctional heterostructure assembly of NiFe
21 LDH nanosheets on NiCoP nanowires for highly efficient and stable overall
22 water splitting. *Adv. Funct. Mater.* **28**, 1706847 (2018).

- 1 46. H.C. Chen, S.P. Jiang, B.H. Xu, C.H. Huang, Y.Z. Hu, Y.L. Qin, M.X. He, H.J.
2 Cao, Sea-urchin-like nickel-cobalt phosphide/phosphate composites as advanced
3 battery materials for hybrid supercapacitors. *J. Mater. Chem. A* **7**, 6241-6249
4 (2019).
- 5 47. Q. Zong, H. Yang, Q.Q. Wang, Q.L. Zhang, Y.L. Zhu, H.Y. Wang, Q.H. Shen,
6 Three-dimensional coral-like NiCoP@C@Ni(OH)₂ core-shell nanoarrays as
7 battery-type electrodes to enhance cycle stability and energy density for hybrid
8 supercapacitors. *Chem. Eng. J.* **361**, 1-11 (2019).
- 9 48. D. Wang, L.B. Kong, M.C. Liu, Y.C. Luo, L. Kang, An approach to preparing
10 Ni-P with different phases for use as supercapacitor electrode materials. *Chem.*
11 *Eur. J.* **21**, 17897-17903 (2015).
- 12 49. X.D. Li, R. Ding, W. Shi, Q.L. Xu, L. Wang, H.X. Jiang, Z. Yang, E.H. Liu,
13 Hierarchical mesoporous Ni-P@MnO₂ composite for high performance
14 supercapacitors. *Mater. Lett.* **187**, 144-147 (2017).
- 15 50. Z. Hu, Z.M. Liu, J.G. Zhao, X.Z. Yu, B.A. Lu, Rose-petals-derived hemispherical
16 micropapillae carbon with cuticular folds for super potassium storage.
17 *Electrochim. Acta.* **368**, 137629 (2021).
- 18 51. S.S. Zheng, Q. Li, H.G. Xue, H. Pang, Q. Xu, A highly alkaline-stable metal
19 oxide@metal-organic framework composite for high-performance
20 electrochemical energy storage. *Natl. Sci. Rev.* **7**, 305-314 (2020).
- 21 52. S.S. Zheng, X.T. Guo, H.G. Xue, K.M. Pan, C.S. Liu, H. Pang, Facile one-pot
22 generation of metal oxide/hydroxide@metal organic framework composites:

- 1 highly efficient bifunctional electrocatalysts for overall water splitting
2 ChemComm. **55**, 10904-10907 (2019).
- 3 53. X. Wang, Y. Fang, B. Shi, F. Huang, F. Rong, R. Que, Three-dimensional
4 NiCo₂O₄@NiCo₂O₄ core-shell nanocones arrays for high-performance
5 supercapacitors. Chem. Eng. J. **344**, 311-319 (2018).
- 6 54. Y.Y. Lan, H.Y. Zhao, Y. Zong, X.H. Li, Y. Sun, J. Feng, Y. Wang, X.L. Zheng, Y.P.
7 Du, Phosphorization boosts the capacitance of mixed metal nanosheet arrays for
8 high performance supercapacitor electrodes. Nanoscale **10**, 11775-11781 (2018).
- 9 55. N. Feng, R.J. Meng, L.H. Zu, Y.T. Feng, C.X. Peng, J.M. Huang, G.L. Liu, B.J.
10 Chen, J.H. Yang, A polymer-direct-intercalation strategy for
11 MoS₂/carbon-derived hetero-aerogels with ultrahigh pseudocapacitance. Nat.
12 Commun. **10**, 1372 (2019).
- 13 56. H.B. Ding, J. Zhou, A.M. Rao, B.A. Lu, Cell-like-carbon-micro-spheres for robust
14 potassium anode. Natl. Sci. Rev. nwaa276, DOI: 10.1093/nsr/nwaa276 (2020).
- 15 57. K. Zhou, W.J. Zhou, L.J. Yang, J. Lu, S. Cheng, W.J. Mai, Z.H. Tang, L.G. Li, S.W.
16 Chen, Ultrahigh-performance pseudocapacitor electrodes based on transition
17 metal phosphide nanosheets array via phosphorization: a general and effective
18 approach. Adv. Funct. Mater. **25**, 7530-7538 (2015).

19
20

21 **Figure captions**

22 **Fig. 1** Schematic illustration for the formation mechanism of flexible hierarchical

1 Ni₂P@Ni(OH)₂@CC electrode

2 **Fig. 2 a** Optical photographs of CC substrate, Ni(OH)₂@CC, Ni₂P@CC and
3 Ni₂P@Ni(OH)₂@CC. **b** Optical photograph shows the flexibility of
4 Ni₂P@Ni(OH)₂@CC electrode. **c** Representative SEM images of
5 Ni₂P@Ni(OH)₂@CC. Inset shows the magnifying image of Ni₂P@Ni(OH)₂ nanosheet
6 arrays on CC substrate. **d** EDS elemental mappings of Ni, P and O in
7 Ni₂P@Ni(OH)₂@CC. **e** TEM and **f** HRTEM images of Ni₂P@Ni(OH)₂ nanosheets
8 scraped off from the CC substrate

9 **Fig. 3** XPS spectra of **a** Ni 2p and **b** P 2p for Ni₂P@CC and Ni₂P@Ni(OH)₂@CC

10 **Fig. 4 a** CV curves of Ni₂P@CC and Ni₂P@Ni(OH)₂@CC electrodes at 5 mV s⁻¹. **b**
11 GCD curves of Ni₂P@CC and Ni₂P@Ni(OH)₂@CC electrodes at 1 mA cm⁻². **c** CV
12 curves of Ni₂P@Ni(OH)₂@CC electrode at different scan rates. **d** GCD curves of
13 Ni₂P@Ni(OH)₂@CC electrodes at different current densities. **e** Areal capacitances
14 and gravimetric capacitances of Ni₂P@CC and Ni₂P@Ni(OH)₂@CC electrodes at
15 various current densities. **f** EIS of Ni₂P@CC and Ni₂P@Ni(OH)₂@CC electrodes.
16 Inset is a view of the high-frequency region

17 **Fig. 5** Relationship between logarithm anodic peak currents and logarithm scan rates

18 **Fig.6** Cycling stabilities of Ni₂P@CC and Ni₂P@Ni(OH)₂@CC at a current density of
19 2 mA cm⁻²

20 **Fig. 7** Ni₂P@Ni(OH)₂@CC//AC hybrid supercapacitors: **a** CV curves at different scan
21 rates. **b** GCD curves at different current densities. **c** The specific capacitances at
22 different current densities. **d** Ragone plots of power density and energy density. **e**

- 1 Cycling stability at 5 mA cm^{-2} for 5000 cycles.

Figures

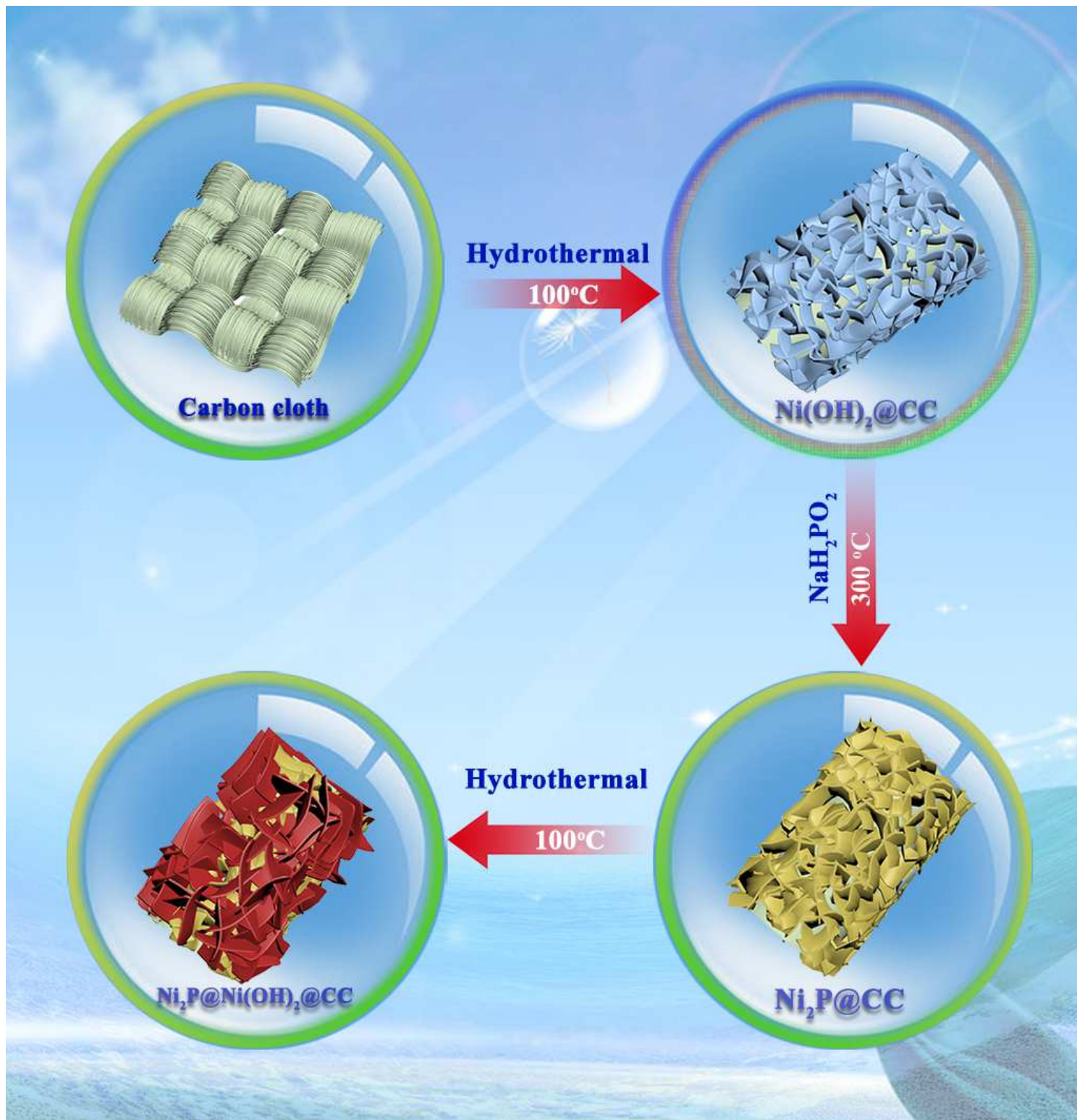


Figure 1

Schematic illustration for the formation mechanism of flexible hierarchical $\text{Ni}_2\text{P}@(\text{Ni}(\text{OH})_2)_2@\text{CC}$ electrode

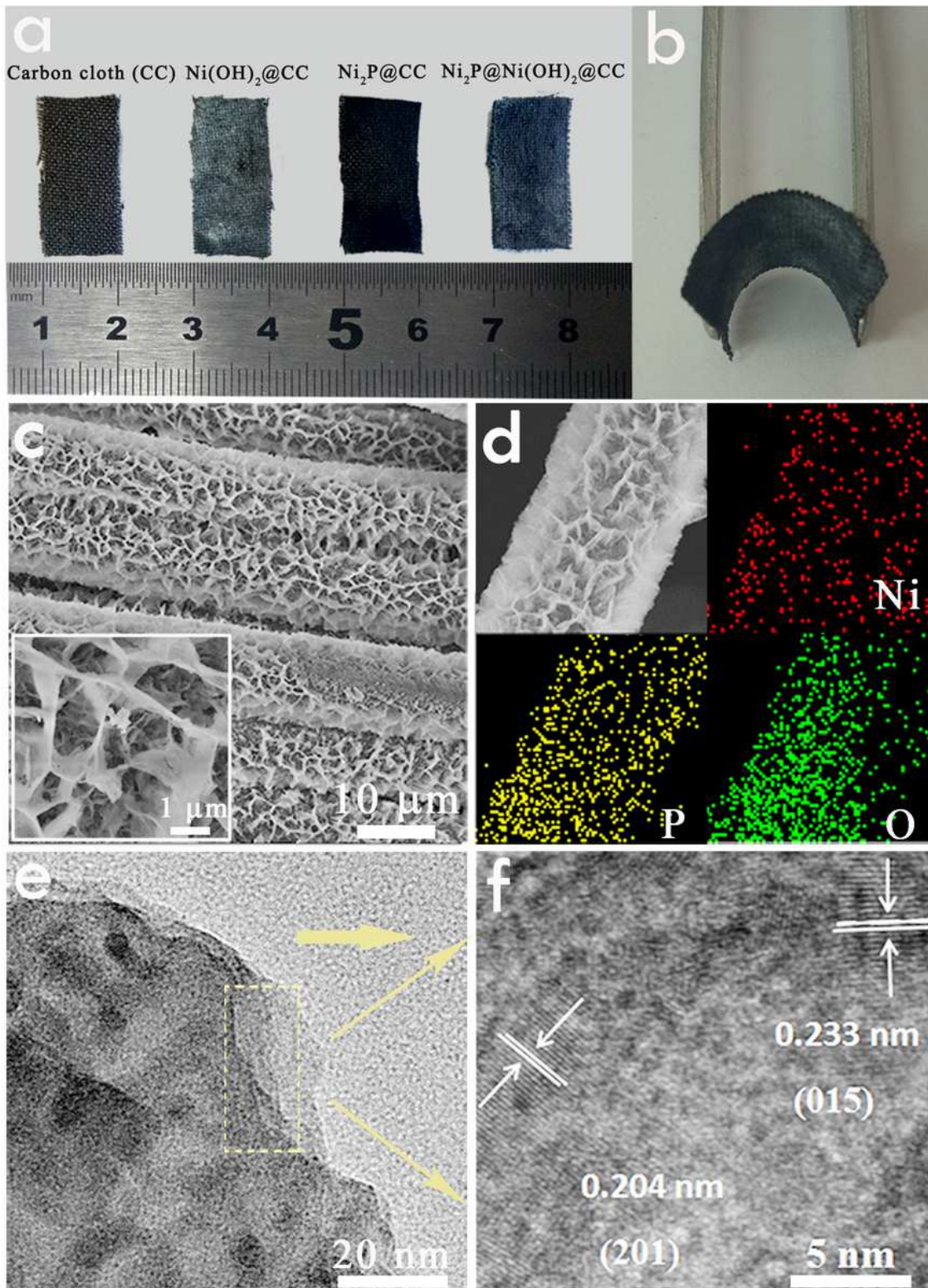


Figure 2

a Optical photographs of CC substrate, Ni(OH)₂@CC, Ni₂P@CC and Ni₂P@Ni(OH)₂@CC. b Optical photograph shows the flexibility of Ni₂P@Ni(OH)₂@CC electrode. c Representative SEM images of Ni₂P@Ni(OH)₂@CC. Inset shows the magnifying image of Ni₂P@Ni(OH)₂ nanosheet arrays on CC substrate. d EDS elemental mappings of Ni, P and O in Ni₂P@Ni(OH)₂@CC. e TEM and f HRTEM images of Ni₂P@Ni(OH)₂ nanosheets scraped off from the CC substrate

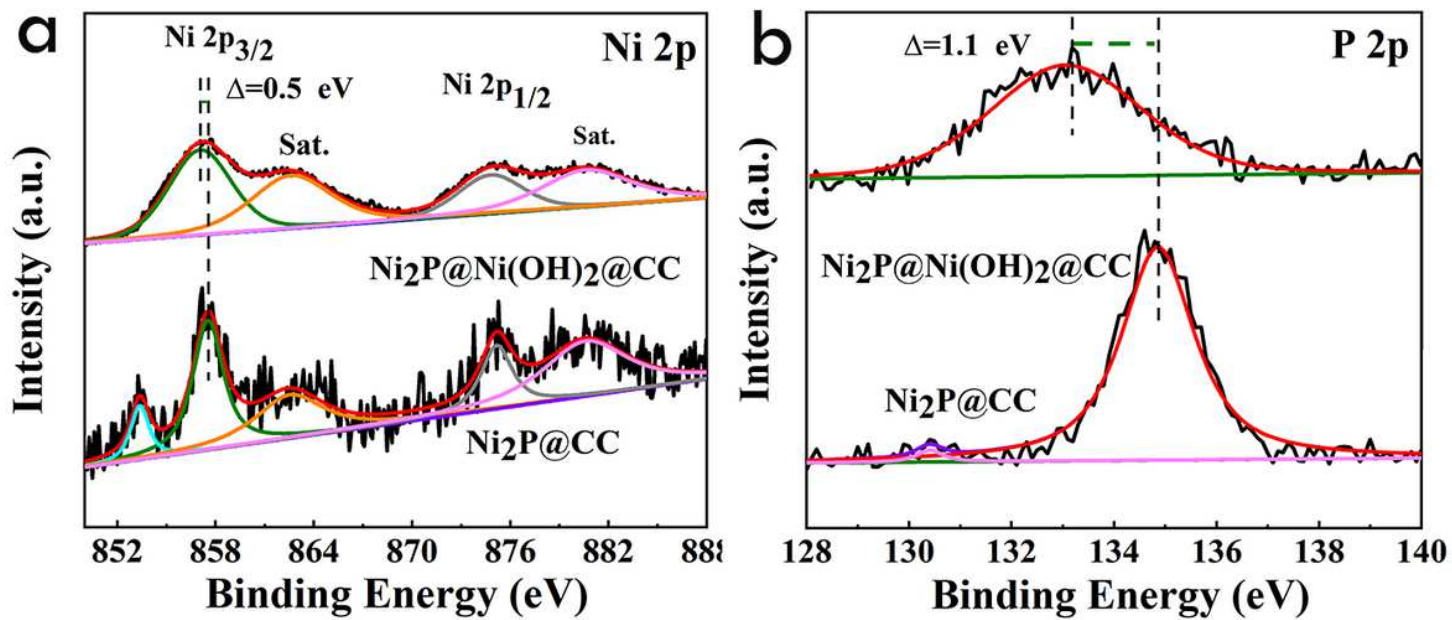


Figure 3

XPS spectra of a Ni 2p and b P 2p for Ni₂P@CC and Ni₂P@Ni(OH)₂@CC

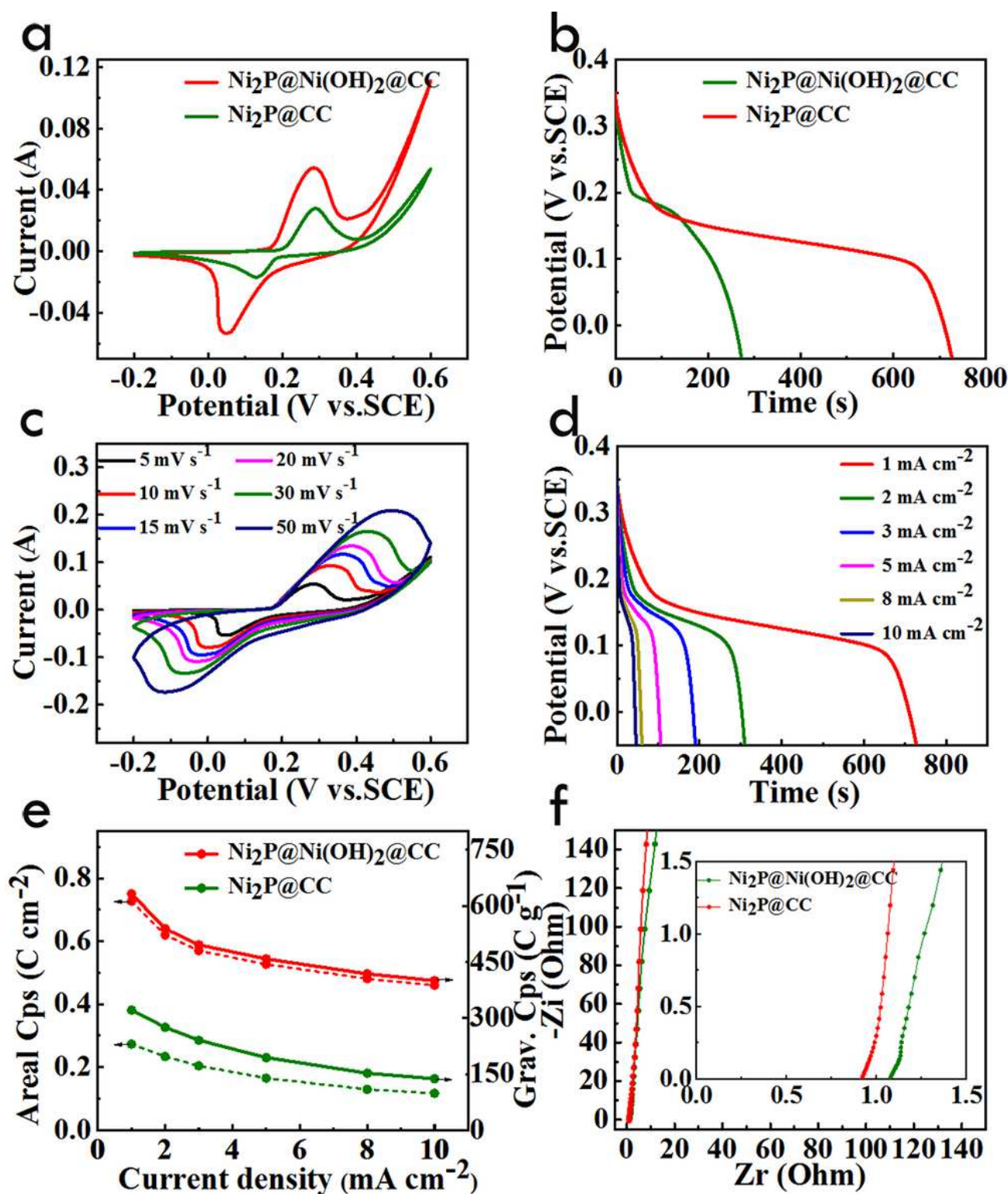


Figure 4

a CV curves of $\text{Ni}_2\text{P}@CC$ and $\text{Ni}_2\text{P}@Ni(OH)_2@CC$ electrodes at 5 mV s^{-1} . b GCD curves of $\text{Ni}_2\text{P}@CC$ and $\text{Ni}_2\text{P}@Ni(OH)_2@CC$ electrodes at 1 mA cm^{-2} . c CV curves of $\text{Ni}_2\text{P}@Ni(OH)_2@CC$ electrode at different scan rates. d GCD curves of $\text{Ni}_2\text{P}@Ni(OH)_2@CC$ electrodes at different current densities. e Areal capacitances and gravimetric capacitances of $\text{Ni}_2\text{P}@CC$ and $\text{Ni}_2\text{P}@Ni(OH)_2@CC$ electrodes at various

current densities. f EIS of Ni₂P@CC and Ni₂P@Ni(OH)₂@CC electrodes. Inset is a view of the high-frequency region

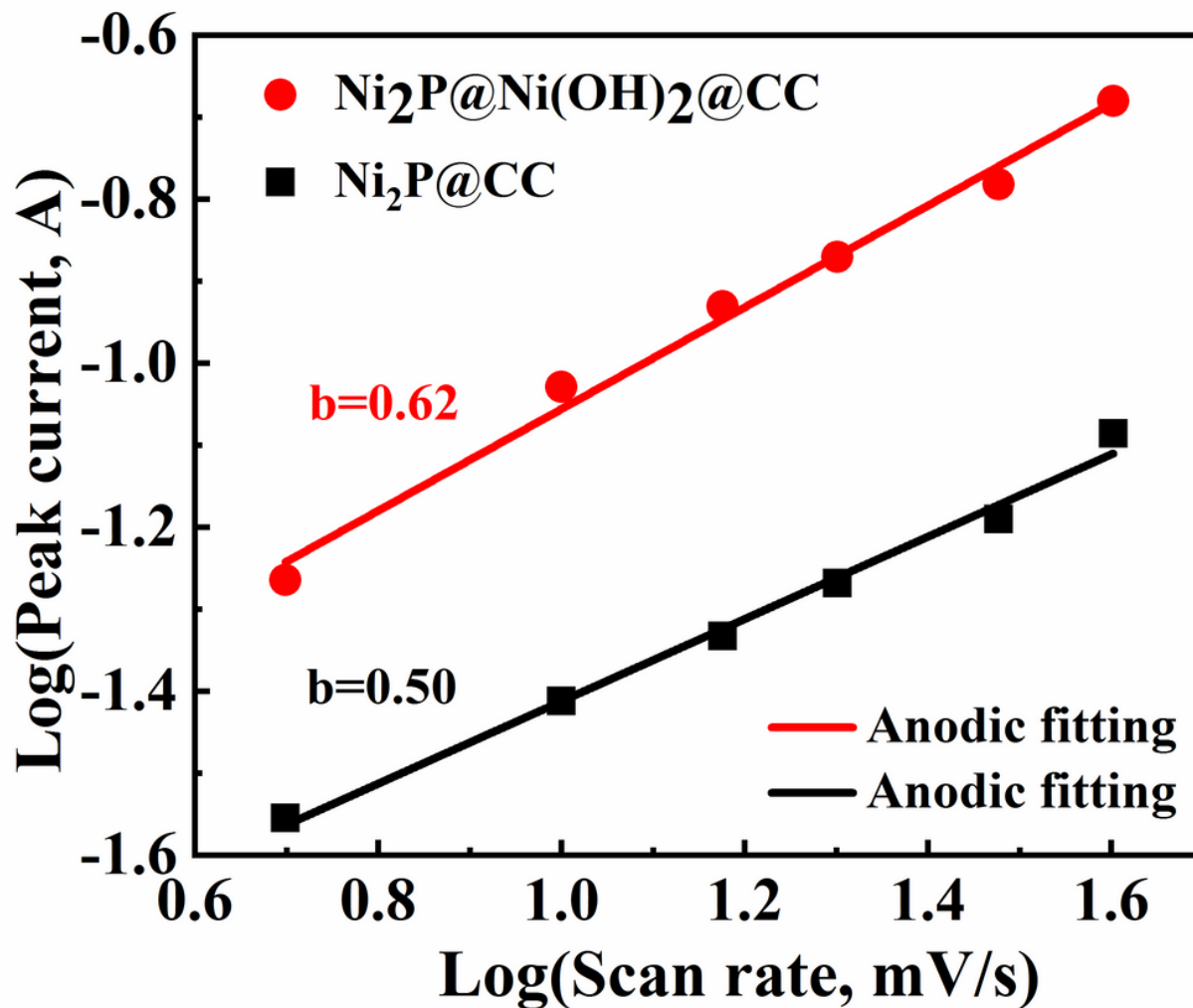


Figure 5

Relationship between logarithm anodic peak currents and logarithm scan rates

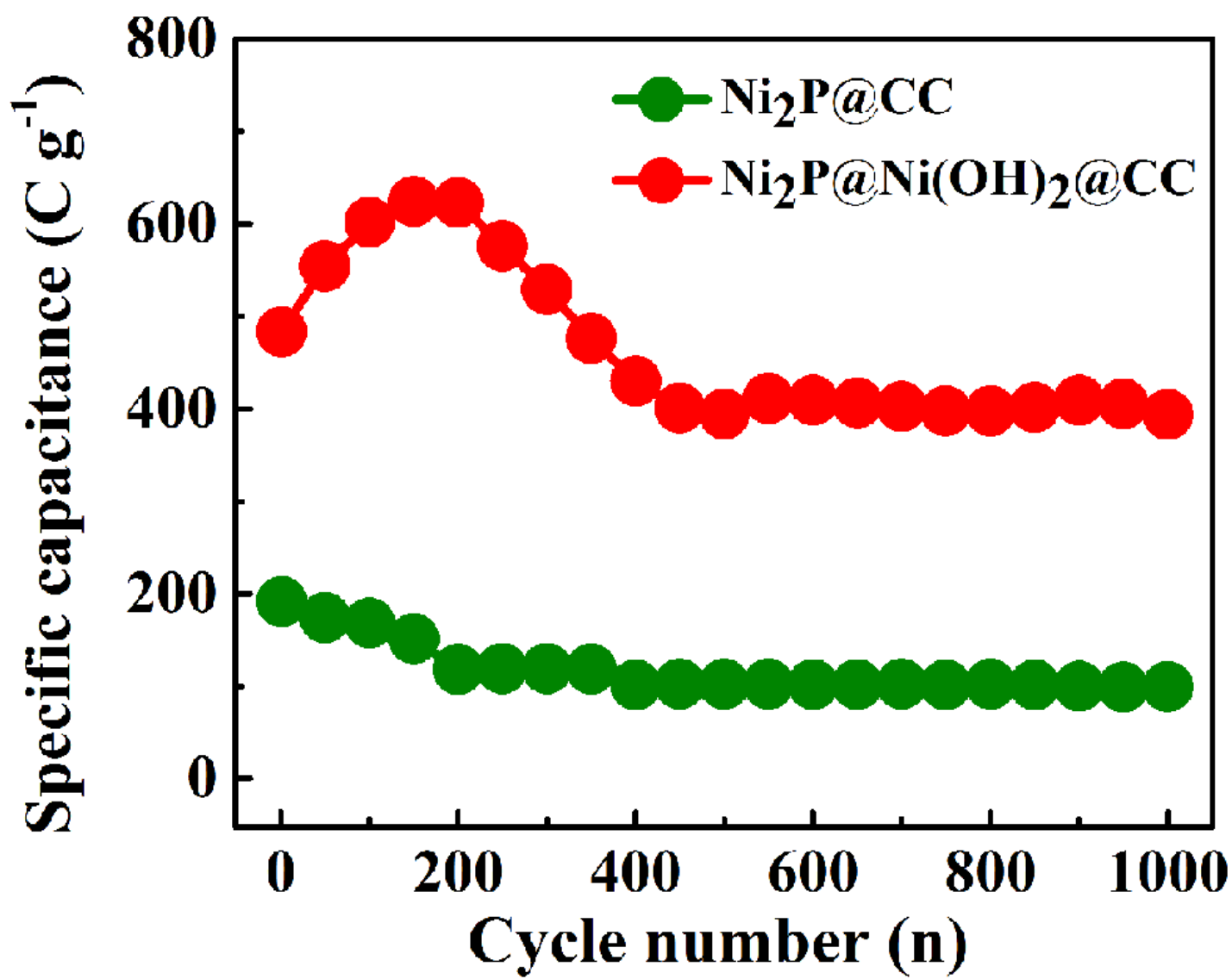


Figure 6

Cycling stabilities of Ni₂P@CC and Ni₂P@Ni(OH)₂@CC at a current density of 2 mA cm⁻²

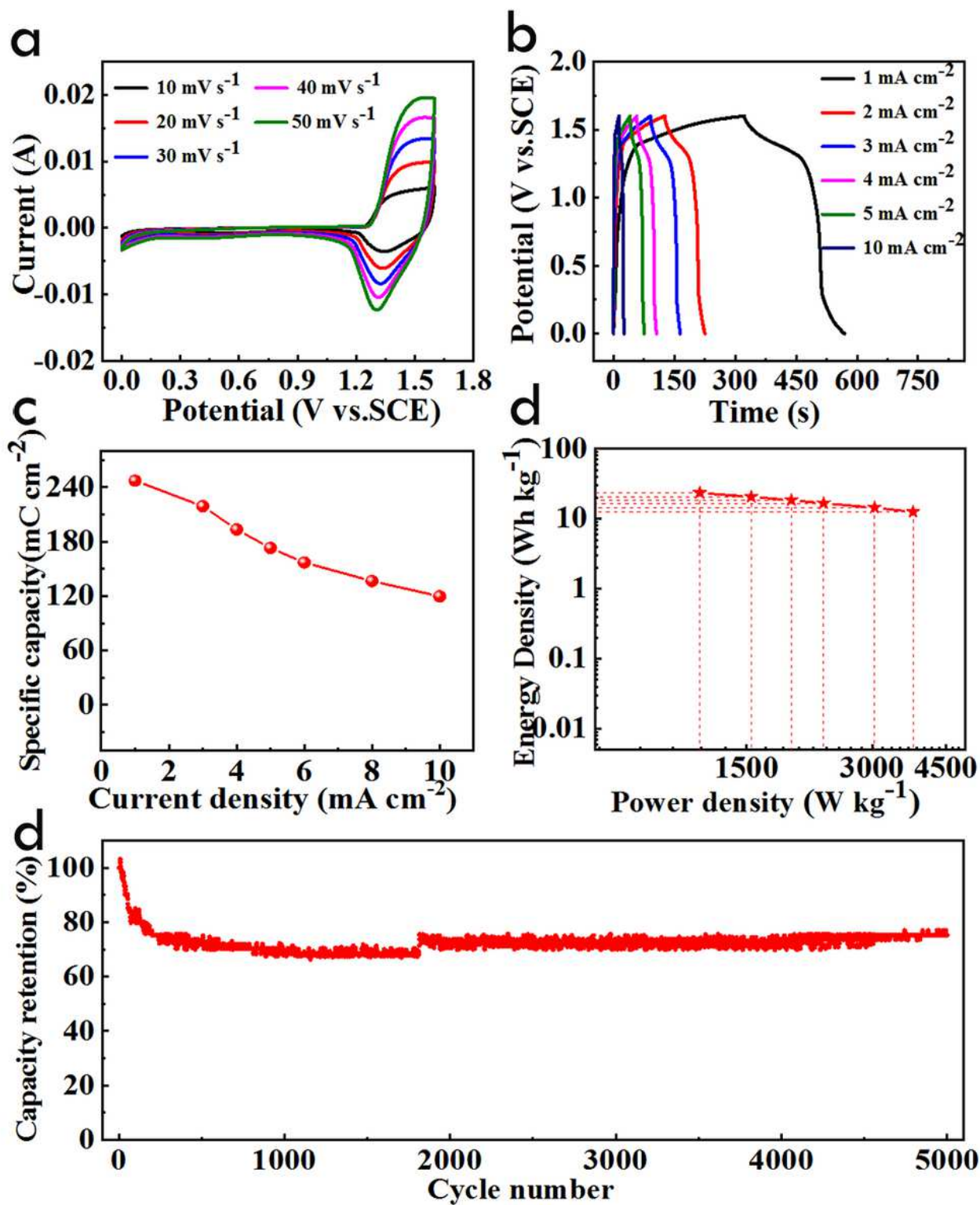


Figure 7

Ni₂P@Ni(OH)₂@CC//AC hybrid supercapacitors: a CV curves at different scan rates. b GCD curves at different current densities. c The specific capacitances at different current densities. d Ragone plots of power density and energy density. e Cycling stability at 5 mA cm⁻² for 5000 cycles.

Supplementary Files

This is a list of supplementary files associated with this preprint. Click to download.

- [SupplementaryMaterial.doc](#)